Medical Physics
The International Journal of Medical Physics Research and Practice

Magnetic cell delivery for peripheral arterial disease: A theoretical framework

Johannes Riegler, Kevin D. Lau, Ana Garcia-Prieto, Anthony N. Price, Toby Richards, Quentin A. Pankhurst, and Mark F. Lythgoe

Citation: Medical Physics **38**, 3932 (2011); doi: 10.1118/1.3593363
View online: http://dx.doi.org/10.1118/1.3593363
View Table of Contents: http://scitation.aip.org/content/aapm/journal/medphys/38/7?ver=pdfcov
Published by the American Association of Physicists in Medicine

Magnetic cell delivery for peripheral arterial disease: A theoretical framework

Johannes Riegler[a)]
Centre for Advanced Biomedical Imaging (CABI), Department of Medicine and Institute of Child Health, University College London (UCL), London WC1E 6DD, United Kingdom and Centre for Mathematics and Physics in the Life Sciences and Experimental Biology (CoMPLEX), UCL, London WC1E 6BT, United Kingdom

Kevin D. Lau
Department for Mechanical Engineering, University College London (UCL), London WC1E 6DD, United Kingdom and Centre for Mathematics and Physics in the Life Sciences and Experimental Biology (CoMPLEX), UCL, London WC1E 6BT, United Kingdom

Ana Garcia-Prieto
Dpto. Fisica Aplicada I, Universidad del Pais Vasco UPV/EHU, Apdo. 644, 48080 Bilbao, Spain

Anthony N. Price
Robert Steiner MRI Unit, Imaging Sciences Department, Hammersmith Hospital Campus, Imperial College London, Du Cane Road, London W12 0HS

Toby Richards
Division of Surgery and Interventional Science, University College Hospital, Grafton Way, London WC1E 5DB, United Kingdom

Quentin A. Pankhurst[b)]
Davy-Faraday Research Laboratory, The Royal Institution of Great Britain, 21 Albemarle Street, London W1S 4BS, United Kingdom

Mark F. Lythgoe[b)]
Centre for Advanced Biomedical Imaging (CABI), Department of Medicine and Institute of Child Health, University College London (UCL), London WC1E 6DD, United Kingdom

(Received 10 February 2011; revised 7 April 2011; accepted for publication 4 May 2011; published 16 June 2011)

Purpose: Our aim was to compare different magnet arrangements for magnetic cell delivery to human lower leg arteries and investigate the theoretical targeting efficiency under realistic flow conditions as a possible treatment after angioplasty. Additionally the potential of scaling down or translating the magnetic actuation device for preclinical studies was explored.
Methods: Using finite element methods, the magnetic field distribution was calculated in 3D for the optimization of magnet arrangements. Computational fluid dynamics simulations were performed for the human posterior tibial artery with the geometry and boundary condition data derived from magnetic resonance imaging (MRI) studies. These simulations were used to trace the trajectories of cells for an optimized magnet arrangement. Additionally the behavior of cells close to the vessel wall was investigated using a fluid-structure interaction model.
Results: The optimal magnet for the lower leg arteries was a Halbach cylinder k3 variety (12 elements with 90° rotation steps for the magnetization orientation). With this magnet, numerical simulations predict a targeting efficiency of 6.25% could be achieved in the posterior tibial artery for cells containing 150 pg iron. Similar simulations, which were scaled down to rabbit dimensions while keeping the forces acting on a cell constant, lead to similar predicted targeting efficiencies. Fluid dynamic and fluid-structure interaction simulations predict that magnetically labeled cells within a 0.5% radii distance to the vessel wall would be attracted and remain at the wall under physiological flow conditions.
Conclusions: First pass capture of magnetically labeled cells under pulsatile flow conditions in human lower leg arteries leads to low targeting efficiencies. However, this can be increased to almost 100% by stopping the blood flow for 5 min. A magnetic actuation device can be designed for animal models that generate magnetic forces achievable for cells in human leg arteries.
 [DOI: 10.1118/1.3593363]

Key words: magnetic cell delivery, Halbach cylinder, peripheral arterial disease, computational fluid dynamics, fluid-structure interaction, magnetic resonance imaging

I. INTRODUCTION

Peripheral arterial disease (PAD) is one of the major manifestations of atherosclerosis leading to the obstruction of blood flow in major arteries, most commonly in the pelvis and legs. Prevalence of PAD is approximately 12% in the United States in people older than 60 years of age, leading to at least 8×10^6 Americans affected.[1] Major risk factors for PAD are similar to those for atherosclerotic diseases in the heart and brain such as advanced age, smoking, diabetes, dislipidema (high blood cholesterol levels) and hypertension. Diabetes further increases the risk for PAD (independent of age) by a factor of 3.[2] With aging populations and a rise in diabetes in the industrialized world, there is an increasing prevalence of PAD.[3] Although PAD is predictive for other cardiovascular events, many patients are asymptomatic as other complications such as stroke or heart disease dictate patient symptomatology.[4] In those who are symptomatic, it presents with progressive cramp in the calves on walking (intermittent claudication).

PAD can lead to critical limb ischemia, particularly in diabetics, where the limb is chronically undersupplied with oxygen and nutrients. Symptoms of critical limb ischemia are rest pain, cold, or numb feet, and nonhealing ulcers or gangrene. Diabetic PAD is the leading cause of amputation in the Western world.

Treatment of PAD includes life style changes, exercise and risk factor modification. Intervention to alleviate symptoms and prevent amputation require the restoration of pulsatile blood flow to the feet.[5,6] This can be achieved via balloon angioplasty, stenting or surgical intervention such as bypass grafting or endarterectomy (surgical removal of a blockage). Catheter based interventions for angioplasty carry lower risks compared to surgery and reduce the duration of hospitalization. However, despite initial improvements in blood flow, long term patency following angioplasty is limited by vascular restenosis and neointimal hyperplasia.[7,8] Neointimal hyperplasia, excessive growth of smooth muscle cells in the blood vessel, is a response of the vessel wall to injury. Several potential solutions for this problem have been suggested including: drug eluting stents,[9] cellular therapies,[10,11] and specific surface coatings for stents,[12] which has lead to some increase in patency.

As traditional techniques are reaching their limits,[9,12] new avenues leading to cellular therapy via specific capture are currently being explored.[13] Drug eluting stents have shown promising results for short term outcome. However, the long term outcome did not improve as vascular healing is delayed.[14] In the last decade, cellular therapies have received more attention particularly since Asahara *et al.*[15] discovered endothelial progenitor cells (EPCs) in the circulating blood. Endothelial progenitor cells are a population of bone marrow-derived cells, which incorporate into sites of neovascularization and endothelial injury. Animal studies indicate that the administration of EPCs to sites of vascular injury leads to re-endothelialization and prolonged vessel patency.[10,11,16] However EPCs are a rare cell type contributing less than 0.0008% of peripheral bone marrow cells in the blood stream,[17] and conventional cell delivery strategies such as interarterial or intravenous infusion retain less than 5% of the cells delivered in coronary arteries.[18] Furthermore, EPC concentrations and activity are reduced in patients with PAD due to the associated risk factors;[19] taken together this results in a suboptimal therapy. There is a clear clinical need to develop a therapeutic strategy to target these cells to the area of need and maximise their retention.

Magnetic cell delivery has been proposed as a potential strategy to improve the cell targeting and retention efficiency. Magnetic cell delivery relies on the fact that human cells contain almost no iron and hence are not actuated by a magnetic field. Yet cells that have been labeled with iron oxide can be directed to a region of interest using a magnetic field with a suitable field gradient. This principle of magnetic targeting has been assessed clinically for drug targeting[20] and preclinically for cell and drug delivery,[21–26] indicating the safety of iron oxide for cell labeling including EPCs.[24,26,27] Theoretical investigations of drug and cell targeting in blood vessels have also been performed.[28–30] Moreover, magnetic labeling of cells has been used for cell tracking with magnetic resonance imaging (MRI) in preclinical models[31] and clinically[32] indicating the safety of transplanting magnetically labeled cells into humans. Labeling of cells with magnetic particles offers the ability of magnetic targeting and non invasive cell tracking of administered cells using magnetic resonance imaging. Although sonography which does not allow tracking of magnetically labeled cells is used more frequently for the diagnosis of PAD, the use of MRI angiograms as primary diagnosis for below knee PAD is increasing. Despite these obvious advantages, no clinical trials for magnetic cell targeting have been conducted.

One of the key reasons for this lies in the nonlinearities of the scalability of magnetic delivery strategies. Magnetic delivery strategies can be divided into three principle groups. The first group uses external permanent magnets to provide a magnetic field and field gradients,[20,33,34] while the second group relies on electromagnets for the same purpose;[21,22,35] the third group uses either permanent magnets or electromagnets to provide a magnetic field and small ferromagnetic implants to generate a field gradient.[25,36] Nevertheless, a common limitation for all strategies is the rapid decline in magnetic field strength and gradient strength with increasing distance from their source. Accordingly, strong magnetic forces can easily be achieved in small animal models but are almost impossible to achieve for human dimensions.

We therefore reason that optimization and feasibility assessment of magnetic cell delivery should start with human dimensions. Following which a scale down to an appropriate animal model[37–39] should be performed, such that the forces acting on cells are kept constant if possible. Following this logic, the aim of this paper is to investigate the theoretical feasibility of magnetic cell delivery to the arteries of the lower leg as a potential supplementary treatment after balloon angioplasty for PAD, in order to improve re-endothelialization and increase vessel patency.

In this study, MRI angiograms were acquired from healthy volunteers, whose leg dimensions were selected to best reflect diabetic patients with PAD. The resulting angiograms were

used to define the position of the three major vessels in the lower leg (peroneal, anterior, and posterior tibial artery) and the skin in 3D. Three-dimensional vessel positions were used for a finite element (FEM) optimization of a range of different magnet configurations in 3D. A computational model of the blood vessels, together with boundary conditions from magnetic resonance phase contrast images were used for computational fluid dynamics (CFD) simulations. This allowed the comparison of the fluid and magnetic forces acting on labeled cells, allowing an estimation of the maximum distance for cells drifting near the vessel wall to be captured by the magnetic field. Moreover, the best performing design was scaled down for a rabbit arterial injury model of the common carotid artery while maintaining a constant force acting on cells.

II. METHODS

II.A. Study subjects

In order to obtain an estimate for the dimensions of diabetic PAD legs, the circumference of legs below the knee, at the maximum Gastrocemius (calf muscle) circumference and above the ankle, were measured from 20 consecutive outpatients (59 ± 12 years, 6 female) who gave their consent. All of these patients had ulcers or gangrene and a history of diabetes mellitus. Informed written consent was obtained from three healthy volunteers (25 ± 4 years, 2 female) for MRI data acquisition to provide an anatomical model of the arteries in the lower leg.

II.B. MRI

Magnetic resonance imaging was performed on a 3T Philips scanner (Best, The Netherlands) using an eight-channel phased-array receive coil. Axial 2D time-of flight angiography images were acquired downstream of the branching of the peroneal and posterior tibial arteries. One hundred consecutive slices were acquired using the following parameters: field of view (FOV) 120×120 mm, slice thickness 2 mm, matrix size 160×160, flip angle (FA) 50°, echo time (TE) 4 ms, repetition time (TR) 21 ms, and reconstructed to $0.25 \times 0.25 \times 2$ mm. 2D phase contrast (velocity encoded) gradient echo images were acquired for the inflow and outflow slice of this volume. Twenty time frames were acquired to cover one cardiac cycle using echocardiography retrospective gating and the following imaging parameters: TR 12 ms, TE 7 ms, number of signal averages (NSA) 3, FA 10°, velocity encoding 80 cm/s, reconstructed to $0.5 \times 0.5 \times 2$ mm.

A sacrificed rabbit (2 kg) was scanned using a 9.4T Varian VNMRS scanner (Palo Alto, CA). Consecutive axial gradient echo slices were acquired to cover the whole neck area with a 72 mm volume coil (Rapid Biomedical, Rimpar, Germany) using the following imaging parameters FOV 60×60 mm, slice thickness 1 mm, Matrix size 512×512, TR 1370 ms, TE 7 ms, and NSA 8, FA 30°.

II.C. Theoretical background for magnetic targeting

Matter can be classified into five basic groups according to their behavior when placed into a magnetic field. The groups that are of concern to us for this paper are ferromagnetic, ferrimagnetic, and paramagnetic materials. Ferromagnetism arises from strong interactions of atomic moments in materials such as iron, nickel and cobalt, and some of their alloys. These materials can maintain their magnetization after the removal of an external magnetic field and are hence used for the manufacturing of permanent magnets. Ferrimagnetic materials show also a strong interaction of atomic moments, but the orientation of these moments is opposing for different crystal lattices. A net moment remains as magnetic moments are not equal for the different lattices. Ferrimagnetism is observed in some crystals consisting of different irons such as magnetite (Fe_2O_3). Paramagnetic materials have magnetic moments that are essentially noninteracting. These materials show no magnetization without an external magnetic field, yet positive magnetization due to the alignment of their magnetic moment with an external magnetic field.

Most particles which are used for magnetic drug targeting are superparamagnetic. If the crystal size of ferromagnetic or ferrimagnetic materials is reduced, so that their magnetic moments can be reorientated by thermal energy, superparamagnetic behavior can be observed. Superparamagnetic particles show a linear increase in magnetization for small external magnetic fields (like paramagnetic materials) but reach a saturation magnetization for higher external field strength (>0.1 T). A magnetization curve shows this relation between magnetization and applied magnetic field. This curve is S-shaped for superparamagnetic particles and the positive quarter of it can be approximated with a Langevin function.

The magnetic force acting on a particles depends essentially on three parameters; the magnetization of the particle, the magnetic field, and its gradient. This can be described by the following equation:[40]

$$F_m = (m \cdot \nabla)B, \tag{1}$$

where m is the magnetic dipole of the particle, and B is the magnetic flux density.

For particles suspended in a medium their magnetic dipole can be replaced via their volume magnetization leading to

$$F_m = \frac{V_m \Delta\chi}{\mu_o}(B \cdot \nabla)B, \tag{2}$$

with V_m as particle volume, $\Delta\chi$ the susceptibility difference between particle and surrounding medium, and μ_0 the permeability of free space. Equation (2) is only correct for low magnetic field strength, where the particle magnetization is linearly dependent on the applied field. However, as mentioned above a Langevin approximation can be used to describe the magnetization of these particles for any field strength

$$L(B) = \coth(\varepsilon) - \frac{1}{\varepsilon} \tag{3}$$

and

$$\varepsilon = \frac{\pi D^3 \mu_o M_s \left|\frac{B}{\mu_0}\right|}{6 k_b T}, \tag{4}$$

where by M_s is the saturation magnetization of the particle, D the particle diameter, T temperature, $\left|\frac{B}{\mu_0}\right|$ magnitude of the magnetic field strength, and k_b Boltzmann's constant. Using Eq. (3), we can rewrite Eq. (2) as

$$F_m = \frac{V_m M_s L(H)}{\mu_0}\left(\frac{B}{|B|}\cdot\nabla\right)B. \tag{5}$$

With Eq. (5) we can calculate the magnetic force for low field strength where the force is proportional to field strength and gradient, as well as for high field strength, where the force is only proportional to the gradient. For magnetic targeting of cells, a scalar for the number of superparamagnetic particles in a cell N, needs to be added to Eq. (5) leading to

$$F_m = \frac{N V_m M_s L(H)}{\mu_0}\left(\frac{B}{|B|}\cdot\nabla\right)B. \tag{6}$$

Magnetic forces acting on a cell were always calculated for cells with an internalized iron oxide concentration of 15 pg/cell unless stated otherwise. The main force that needs to be overcome for the targeting of suspended cells is the drag force of the fluid,

$$F_d = -6\pi\eta R_c(v_c - v_f), \tag{7}$$

where R_c is the cell radius, η the dynamic viscosity, and $v_c - v_f$ is the velocity difference between cell and fluid. Equation (7) is Stokes drag force, which is only accurate for low Reynolds numbers as commonly found for magnetic cell targeting. Furthermore, Eqs. (6) and (7) do not include dipole–dipole interactions, buoyancy forces, gravitational forces, and Brownian motion, which can be important under some circumstances.

II.D. Magnet optimization using finite element methods

Permanent magnets offer high field strength without the need for electric power or cooling. However, as there are many potential arrangements, a rational optimization is necessary.

We used commercially available finite element modelling software OPERA v12, TOSCA (Kidlington, UK) to calculate the magnetic field distribution in three dimensions for four basic geometries: Halbach cylinder (in this paper always a hollow cylinder), linear Halbach array, equilateral triangular rod and magnetic rod (see Fig. 1). In order to test for mesh independence of our finite element simulations, all element sizes were halved for one simulation for each geometry, which lead to an error in the magnetic force of $<0.7\%$ on average.

The Halbach cylinder is a one sided flux concentrator with continuously changing magnetization direction[41] (ϕ) following:

$$\varphi = k\phi, \tag{8}$$

with k as a positive integer between 2 and 4 for internal flux concentration, and ϕ the angle for the position around a circle. However, as this would be difficult to build, in practice

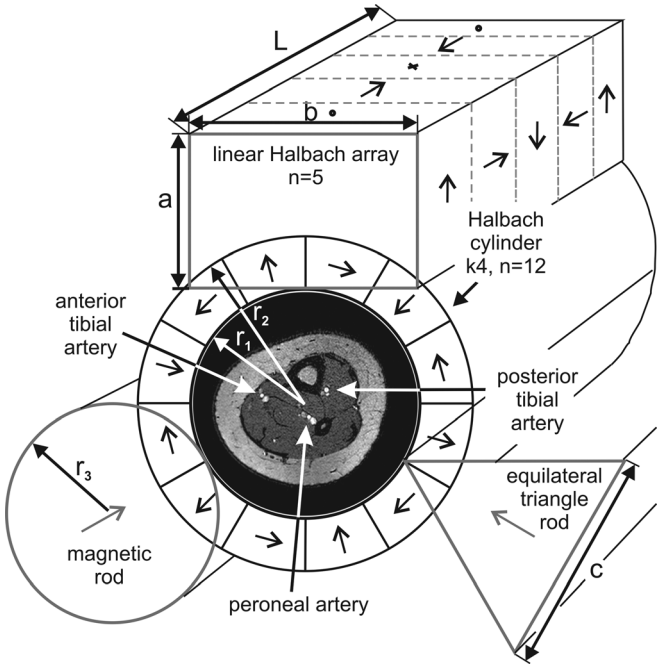

FIG. 1. Geometrical arrangement of different magnet shapes around a human leg. A magnetic resonance image is shown in the center of the Halbach cylinder to indicate the three major blood vessels of the lower leg. Open arrows indicated the magnetization orientation of different elements. Note that only one of the basic geometries was used at one time for finite element simulations.

Halbach cylinders are built out of segments with a constant magnetization using Eq. (8) for the center of each element. This leads to a reduction of the flux density[41] following:

$$\mathrm{B(n)} = B_c\frac{\sin(2\pi/\mathrm{n})}{2\pi/\mathrm{n}}, \tag{9}$$

where B_c stands for the magnetization of a Halbach cylinder with continuously changing magnetization orientation and n for the number of elements.

A linear Halbach array is also a one sided flux concentrator, which follows the same principle as the Halbach cylinder (magnets with sinusoidal magnetization produce single sided fields). The magnetization orientation makes one full rotation along L (one wavelength) focusing all magnetization on the lower side of the array.

For each of the four geometries tested, the magnets were arranged around an air cylinder (placeholder for a human leg) with a radius of $r_1 = 80$ mm and a length of $L = 200$ mm (for a full list of model parameters see Table I) while r_2, r_3, c, and a (see Fig. 1) were increased to calculate the magnetic field for an increasing magnet volume. An MRI angiogram of a leg was centered in the air volume to get blood vessel positions in 3D space. For each of the three vessels considered, magnetic forces acting on cells in the center of them were calculated at 20 points along their centerline. Magnets arranged around the air cylinder were rotated 360° around its long axis in 36 steps. Forces acting on cells for 60 points (20 points, 3 blood vessels) of each rotation step were evaluated. The rotation which generated the highest force over all 60 points was selected and the resulting average has been used

TABLE I. Physical parameters used for this manuscript.

Parameter	Symbol	Value	Units
Length for magnets and vessel section	L	200 (200–300)[a], 40[b]	mm
Halbach cylinder inner radius	r_1	80 (54–98)[a], 25[b]	mm
Halbach cylinder outer radius	r_2	140 (82–240)[a], 29[b]	mm
Magnetic rod radius	r_3	115 (18–226)[a]	mm
Linear Halbach array height	a	259 (6–1005)[a]	mm
Linear Halbach array width	b	160 (40–160)[a]	mm
Equilateral triangle side length	c	309 (75–609)[a]	mm
Outer radius endplate	r_4	130 (100–140)[a]	mm
Endplate angle	α	45 (30–90)[a]	°
Endplate hight	h	25 (5–50)[a]	mm
Residual flux density NdFeB[c]	B_r	1.36	T
Coercivity NdFeB[c]	H_c	1051	kA m^{-1}
Relative permeability NdFeB[c]	μ_r	1.04	—
Residual flux density sintered ferrite	B_r	0.37[b]	T
Coercivity sintered ferrite	H_c	240[b]	kA m-1
Relative permeability sintered ferrite	μ_r	1.21[b]	—
SPION[d] crystal size	D	8.8	nm
Saturation magnetization iron oxide	M_s	354	kA m^{-1}
Temperature	T	300	K
Magnetic permeability free space	μ_0	$4 \times \pi \times 10^{-7}$	H m^{-1}
Boltzmann constant	k_b	1.38×10^{-23}	J K^{-1}
Cell radius	R_c	10	μm
Cell density	ϕ_c	1100	kg m^{-3}
Cells Young's modulus	—	10	kPa
Cells Poisson ratio	—	0.45	—
Dynamic viscosity, fluid	η	0.0039	kg m s^{-1}
Fluid density	ϕ_f	1080	kg m^{-3}

[a]The first number indicates dimensions which were used for the comparison of magnet arrangements with the same volume, while numbers in brackets indicate the range used for simulations.
[b]Numbers indicate values used for the rabbit scale model.
[c]NdFeB Neodymium Iron Boron.
[d]SPION superparamagnetic iron oxide nanoparticles.

for average force plots. Force calculations were performed using MATLAB (R2010a, Natick, MA).

All of these geometries, except for the Halbach cylinders have a one sided distribution of magnet material. In order to investigate different arrangements of the basic geometries, a magnet volume was selected (6600 cm^3) and kept constant while the number of basic geometric elements (linear arrays, rods, triangular rods) around the air cylinder was increased. For example 1, 2, 4, 6, 8, 10, and 12 magnetic rods were equally spaced around the air cylinder, while r_3 was decreased to keep the total magnet volume constant. The magnetization was orientated toward the center for $n=1$, following a dipole orientation for $n>1$ and following a quadrupole orientation for $n>4$ as given by

$$\varphi = (1 + (p/2))\phi, \tag{10}$$

with $p=2$ for a dipole and $p=4$ for a quadrupole.

For the Halbach cylinders, a k3 variety was used with decreasing n leading to a magnetic hollow cylinder with a single magnetization orientation for $n=1$. Magnetization orientations for the linear Halbach array were kept constant, but a and b were adjusted in order to fit n linear arrays around the air cylinder.

To address the scalability of a Halbach cylinder k3 for a range of potential human leg diameters, the ratio of r_1/r_2 was kept at 0.62 while r_1 was increased from 54 to 98 mm.

All of these simulations were done in 3D using the demagnetization curve of commercially available neodymium–iron–boron magnet standard grade 45SH (remanence magnetization $B_r=1.36$ T, coercivity $H_c=1051$ kA/m, and relative permeability $\mu_r=1.04$).[42]

Finally, simulations for the scale down of a Halbach cylinder k3 for a rabbit common carotid artery model, with $r_1=25$ mm and $L=40$ mm, were performed using the demagnetization curve of commercially available magnetic sintered ferrite ($B_r=0.37$ T, $H_c=240$ kA/m, $\mu_r=1.21$).[43]

II.E. Model construction for computational fluid dynamics

In this study, the geometry of the arterial system has been simplified from a three-dimensional tube to a two dimensional channel in order to reduce the computational cost of the simulations. The geometry has been taken as a channel section 2.2 mm in diameter (according to the MR angiogram); 200 mm in length and 0.11 mm in width (see Fig. 9). The fluid has been modeled as incompressible Newtonian fluid with a density of 1080 kg m^{-3} and a viscosity of 0.0039 kg m s^{-1} (density and viscosity of blood). The volume was meshed using mixed tetrahedral and hexahedral elements (Fig. 9) and was tested for mesh independence by applying a constant velocity boundary condition at the inlet of 0.25 m s^{-1} (maximum difference between inflow and outflow boundary value), 0 Pa pressure at the outlet and symmetry boundary conditions enforcing the two-dimensional flow. Velocity variations down the center of the channel were assessed, and the mesh was determined sufficiently fine when the maximum percentage difference between successively finer meshes was found to be less than 1%. The final mesh consisted of 156 155 nodes and 419 191 elements.

Flow profiles were extracted from phase contrast images using the freely available software segment.[44,45] The average velocity recorded at both inlet and outlet was fitted to an eighth order Fourier series using MATLAB. These were then applied to the fluid domain as inlet and outlet velocity boundary for the channel.

For the rabbit common carotid artery, a channel diameter of 1.5 mm, a length of 30 mm, and a width of 0.11 mm were used. For the inflow boundary, an interpolated spline fit was performed using MATLAB with the flow profile from Cui *et al.*,[46] while the outflow pressure boundary was set to 0 Pa.

II.F. CFD simulations and post processing

Computational fluid dynamics modeling was performed using ANSYS CFX 11.0, a finite volume based computation fluid dynamic solver, which solves the unsteady equations for mass and momentum conservation of an incompressible fluid. The unsteady flow dynamics are solved by advancing the solution with a time steps of 0.01 s. At each time step, the residuals of the nonlinear system are reduced till either the maximum of the residuals of both the velocities and

pressures were less than 10^{-6} or 100 convergent iterations had been performed. In order to assess the periodicity of the solution, the boundary conditions were repeated for three cardiac cycles.

Postprocessing of this data was performed using ENSIGHT 9.1.2, which was used to model particle traces under the application of magnetic forces. Cells were simulated as massed particles (m_p), which experience drag (F_d) and magnetic forces (F_m),

$$m_p \frac{d_v}{d_t} = F_d + F_m. \tag{11}$$

Constant magnetic forces between 12 and 120 pN were applied corresponding to an iron load of 15–150 pg/cell. The path of each magnetically labeled cell was traced at each time step, displaying how the particle path would evolve under both fluid and magnetic forces.

II.G. Behavior of a cell close to the arterial wall

A fluid-structure interaction model was used to model the behavior of a cell near a vessel wall. As this requires both the structural deformation and fluid-structure interaction, the explicit finite element code LS-DYNA was used. A cell was modeled as an isotropic elastic body with a density of 1100 kg m^{-3}, Young's modulus of 10 kPa, and a Poisson ratio of 0.45. A commonly reported Young's modulus for human umbilical vein endothelia cells[47] was chosen as no data for EPCs could be found.

A uniform inlet velocity of 0.01 m s^{-1} was applied, which corresponds to the maximum value of the velocity at the top of the fluid domain assuming that the full velocity profile in the channel is parabolic. The simulations were run until a linear velocity gradient was formed across the inlet. Magnetic forces were applied to the cell by applying a uniform and constant force to each node in the cell, pulling it toward the wall.

Fluid-structure interaction was performed using a penalty coupling method, whereby the force applied to both fluid and structural domains was determined by calculating the level of fluid penetration into the solid domain. The fluid model of LS-DYNA is a compressible model and was defined with the following parameters: density 1080 kg m^{-3}, dynamic viscosity 0.0039 Pa s, and a bulk modulus of 22 GPa. The value of the bulk modulus directly controls maximum timestep in explicit time integration, thus in order to obtain simulations that runs in reasonable time frames this value was reduced to 1% of its true value, which was found to have no effect by comparing the numerical solution to the analytical solution of channel flow.

III. RESULTS

III.A. Magnet optimization

The maximum calf muscle radius measured for our patient group was 98 mm (see Table II). We therefore choose a radius of 80 mm for our initial comparison of different magnet arrangements, as these would accommodate 90% of our population. As our patient group is limited, it may not reflect the real variability of PAD patients; we therefore investigated the scalability of a magnet in Sec. III B. Figure 2 shows the average magnetic force acting on cells in the anterior tibial artery, posterior tibial artery, and peroneal artery, for six magnet arrangements, with increasing magnet volume. For magnet volumes below 1000 cm^3, the magnetic rod, the Halbach cylinder k3 and the linear Halbach array generate a similar force. However, for larger magnet volumes, the Halbach cylinder k3 generates a stronger magnetic force than any other arrangement, followed by the Halbach cylinder k2. No change in magnetic force was notable above 10000 cm^3 from the magnetic triangle, magnetic rod, linear Halbach array or Halbach cylinder k4.

Figure 3 shows the effect of multiple elements of basic magnet arrangements on the average magnetic force acting on a cell. The Halbach cylinder k3 again outperforms all other arrangements, provided it is constructed of more than six elements [see Eq. (9)]. For less than six elements, the magnetic rods are superior, closely followed by linear Halbach arrays. A quadrupole arrangement [see Eq. (10)] of magnetic rods comes closest to the Halbach cylinder k3 for more than six elements.

Figure 4 shows the force profile for a linear Halbach array and for the Halbach cylinders k3 and k4 across the center of

TABLE II. Leg dimensions for a small group of patients with peripheral arterial disease.

$n = 40$	Radius below knee	Maximum radius	Radius above ankle	Radius ankle
mean ± SD (mm)	59 ± 10	60 ± 11	38 ± 7	43 ± 5
minimum (mm)	37	46	25	35
maximum (mm)	91	99	59	59

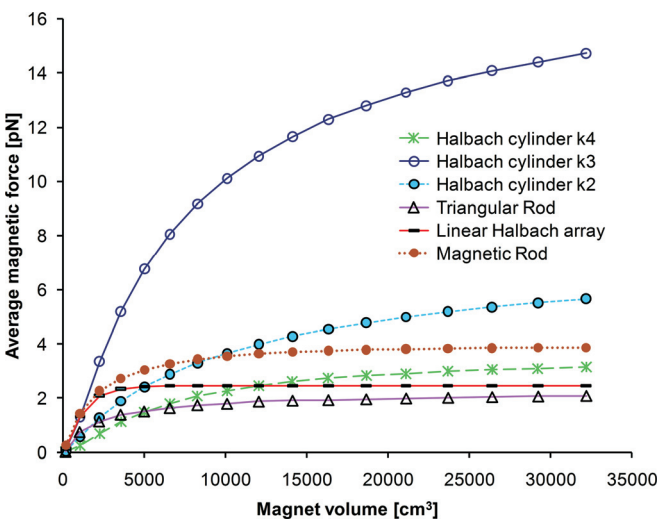

FIG. 2. Average forces acting on magnetically labeled cells in the three major arteries of the human leg for different magnet arrangements with increasing magnet volume. All Halbach cylinders consisted of 12 elements while one magnetic rod and triangular magnetic rod were used. The linear Halbach array consisted of five elements.

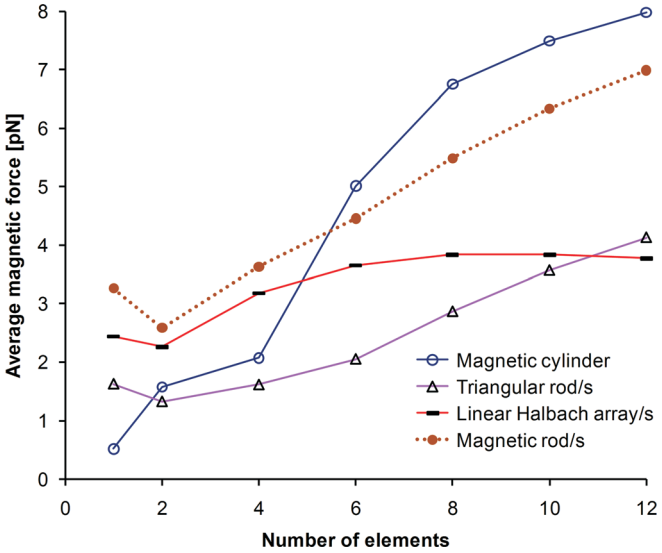

FIG. 3. Average magnetic force produced by an increasing number of the basic geometrical magnet arrangements arranged symmetrically around the leg. The magnet volume is constant (6600 cm^3) for all of these arrangements. Note that for the Halbach cylinder/magnetic cylinder, the cylinder was not modified; only the number of elements it was divided into was changed. As outlined in Sec. II D, the magnetization orientation of the Halbach cylinder follows k3 for more than six elements.

the air cylinder. Radial distances for blood vessels from the center axis of the leg are shown as well to visualise the expected force for such radii. The mean distance between anterior tibial artery, posterior tibial artery, peroneal artery, and the skin for three angiograms was 32 ± 7 mm. Note that the force produced by cylindrical magnet arrangements is rotationally symmetric, while the force from the linear array continues to fall with increasing distance. The Halbach cylinder k3 produces a fairly constant force over a wide range of its internal radii due to its linear field gradient profile.

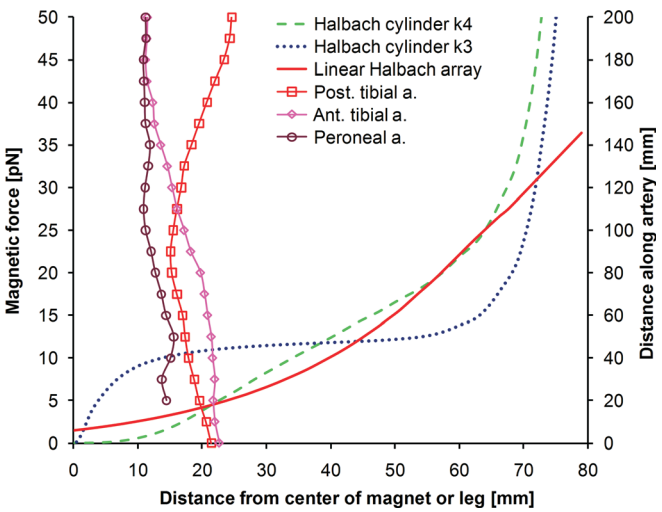

FIG. 4. Example force profiles for different magnets using the same volume of magnetic material (6600 cm^3) All Halbach cylinders consist of 12 elements while the linear Halbach array consists of five elements. The radial position of the major lower leg arteries have been plotted to indicate their position within the magnet.

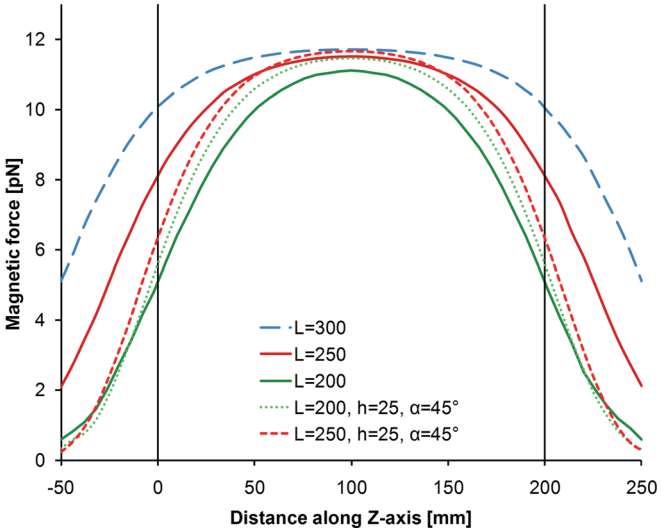

FIG. 5. Linearity of the magnetic force along the z-axis of k3 Halbach cylinders with different lengths and endplates. The definition of the endplate height and the circumferential angle α are shown in Fig. 6.

An infinite Halbach cylinder would have a perfectly symmetric field distribution. However, the finite length of real cylinders leads to flux loss at the ends and hence to decreased field and gradient strength. Figure 5 shows a comparison of different cylinder lengths for Halbach cylinders k3. Additionally, the effect of endplates as outlined by Bjørk *et al.*[48] has been assessed. Vertical black lines have been drawn in Fig. 5 to indicate the length of the blood vessel segments used for CFD simulations. All force profiles shown in this figure are for a line with a radius of 15 mm away from the center. Increasing the cylinder length beyond the length of the vessel segment leads to considerable improvements in the homogeneity of the force. The use of endplates as indicated in Fig. 6 has the benefit of minimising the use of magnetic material while increasing the force acting along the line. However, the linearity was not improved to the same degree as for the extended Halbach cylinders.

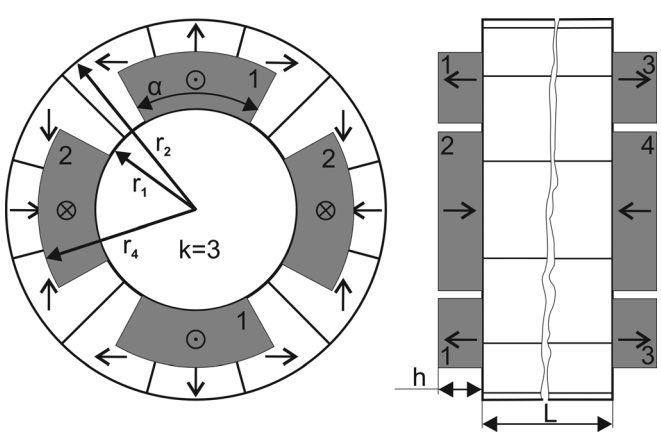

FIG. 6. Geometrical arrangement of endplates on a Halbach cylinder k3. Endplates are made of the same magnetic material as the Halbach cylinder. Open arrows have been used to indicated the magnetization orientation of the four endplates.

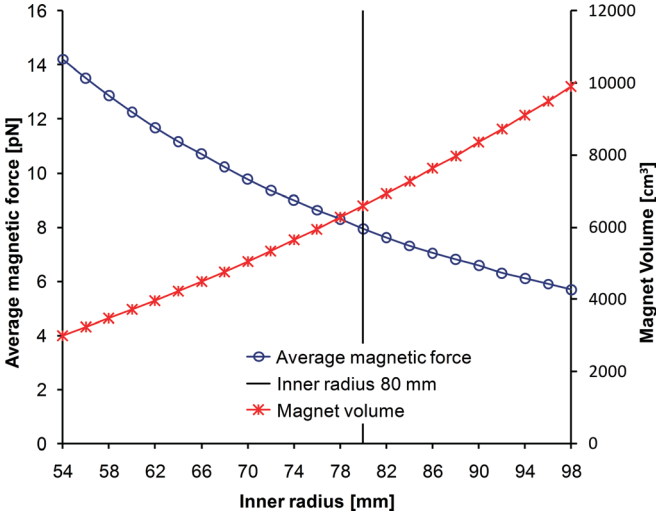

FIG. 7. Average magnetic forces produced by Halbach cylinders k3 with different inner diameters illustrating the scalability for different human leg diameters. A constant ratio between inner and outer diameter of 0.62 was used for all Halbach cylinders. The black horizontal line indicates an inner radius of 80 mm corresponding to the sixth circle on the Halbach cylinder k3 line of figure 2.

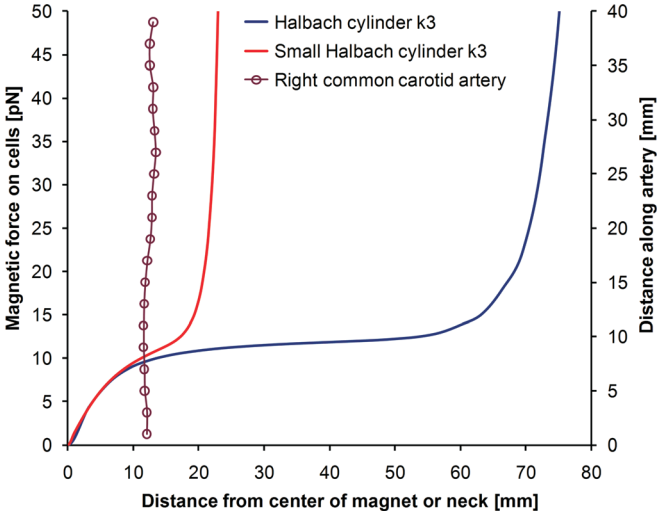

FIG. 8. Force profile for a Halbach cylinder k3 and a scaled down version for a rabbit injury model. The radial position of the right common carotid artery has been plotted to indicate the force cells would experience along the centerline of the artery.

III.B. Scalability of magnetic forces

Two aspects of scalability are addressed in this paper; firstly changing the inner diameter of a Halbach cylinder k3 to accommodate different human leg diameters and secondly the scale down for an animal model.

Figure 7 shows the slow decline of the magnetic force as the inner radius is increased from 54 to 98 mm for Halbach cylinders k3 with a r_1/r_2 ratio of 0.62. Magnetic forces acting on cells for increasing leg diameters decrease from 14 to 6 pN. At the same time, the necessary magnet volume increases from 4000 to 100 00 cm^3.

Figure 8 shows the force profiles along the radius for two Halbach cylinders k3. The first one has an inner radius of 80 mm and is made of neodynium–iron–boron, while the second one has an inner radius of 25 mm and is made of sintered ferrite. The outer radius of the smaller cylinder has been adjusted in order to match the force acting on cells of the bigger cylinder. As the smaller cylinder is intended for a rabbit common carotid injury model, the radial distance of the right carotid from the neck center line has been added. It can be appreciated that the forces acting on cells in the carotid artery would be similar to forces expected for the human lower leg arteries (see Fig. 4).

III.C. Magnetic attraction of cells to the arterial wall

Computational fluid dynamics modeling was used to investigate the behavior of magnetically labeled cells in an artery with pulsatile flow and an external magnetic field. Figure 9 shows a small section of the mesh in the flow channel (approximation for the posterior tibial artery) and seed points, which were used to release and track the movement of cells. Cells were seeded 20 mm inward of the flow channel to avoid disturbances from the inlet.

Figures 10(a) and 10(c) show the trajectories for cells experiencing a magnetic force of 48 pN (60 pg iron/cell) during maximum forward flow (A: toward foot) and backward flow (C; toward knee), respectively. Cells which are within 1% of the chamber radius from the wall will hit the wall, while cells released at 2.5% from the wall will not. Figures 10(b) and 10(d) show the trajectories for cells exposed to a magnetic force of 120 pN (150 pg iron/cell) along the x axis (up) as for A and C. Cells seeded at 0.5 and 1% from the wall contact the wall quickly (in one forward cycle) while cells seeded at 2.5% require both forward and backward cycles to contact the wall. For this case the total capture efficiency over one cardiac cycle would be 6.25% of all cells passing through the channel while a magnetic force of 12 pN per cell would lead to a capture efficiency of $<0.5\%$.

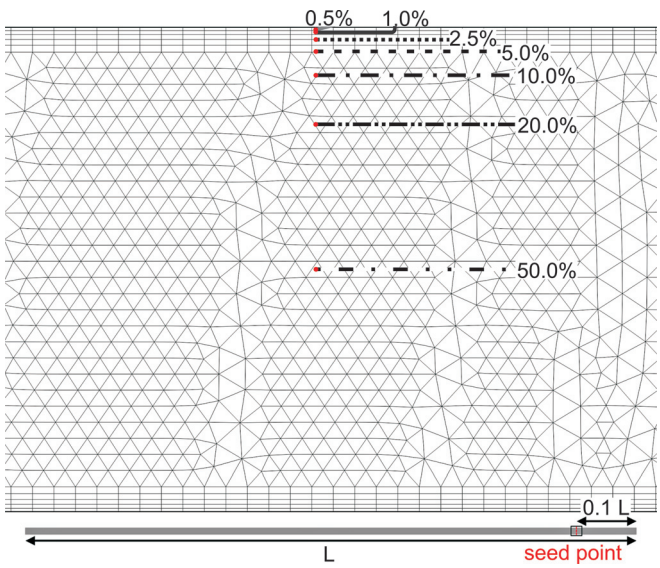

FIG. 9. Close up of the meshed artery channel with the different cell seeding points indicated by full circles at the start of the dashed lines. The size of this section with respect to the whole artery channel is indicated by the box at the bottom of the figure.

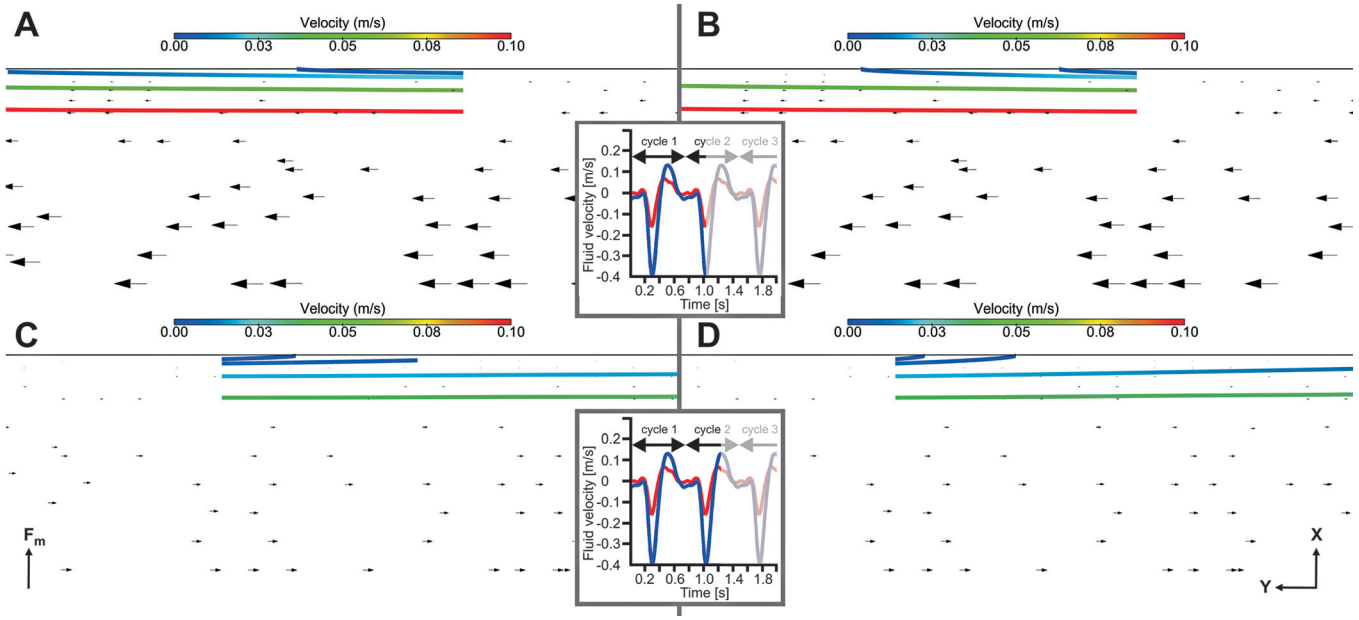

FIG. 10. Trajectories for cells labeled with 60 pg iron per cell at the time of maximum forward flow (A) (toward the foot) and maximum backflow (C) are shown. (B) and (D) show the trajectories for cells labeled with 150 pg iron per cell. The magnetic force is orientated up for all plots, as indicated by the arrow in the lower left corner. Other arrow heads indicate the velocity of the fluid, which are scaled in magnitude. The two plots in the middle show the inflow and outflow profile for a 200 mm anterior tibial artery section over three cardiac cycles, the current time point of the simulations indicated by the difference in shading. Plots A-B show the flow field 1 s after the first heart beat, while C-D show the flow field 1.3 s after the first heart beat.

The plots in the center between A-B and C-D show the flow profile for the inflow and outflow, which have been used in these simulations; these were obtained from a 200 mm section of the posterior tibial artery from a single volunteer. Portions of these flow curves have been shaded to indicate the time points within a cardiac cycle for which the flow profiles are shown.

Capture efficiencies for magnetically labeled cells in the rabbit common carotid artery with an applied magnetic force of 12 and 120 pN per cell were <0.5 and 100% over one cardiac cycle, respectively (data not shown).

III.D. Physical behavior of a cell close to the arterial wall

Fluid-structure interaction simulations were performed to investigate the behavior of a magnetically labeled cell close to the arterial wall as the resolution of the CFD simulations are insufficient to address this issue. A uniform magnetic force was applied on all nodes of the structural model of the cell, while a constant boundary condition was applied for the fluid flow and allowed to evolve.

Figure 11 shows the mesh and the geometrical arrangement at the start of the simulation with the cell at 5 μm from the vessel wall. The magnetic force pulls the cell to the wall (contact occurs in <0.05 ms) and together with fluid forces this leads to the flattening of the cell. Here friction between the cell surface and the wall has been neglected, which results in the cell rolling with minimal displacement along the channel ($\sim$3 μm over 1 s). A snapshot for the fluid field at the rolling condition is shown in Fig. 12 and a movie for the whole process as supplementary movie 1.

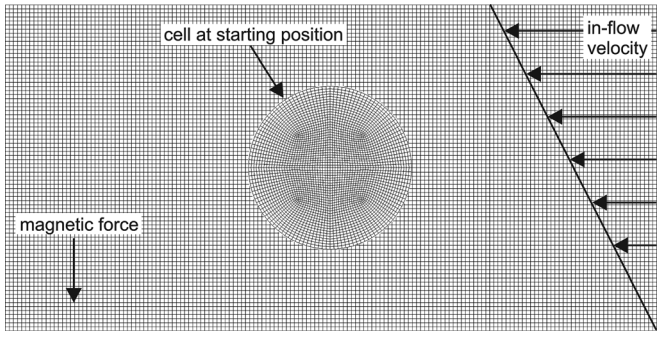

FIG. 11. Finite element mesh of the cell (structure) and fluid used for fluid-structure interaction simulations. A constant fluid velocity is applied on the right side. Here the magnetic force is orientated downwards.

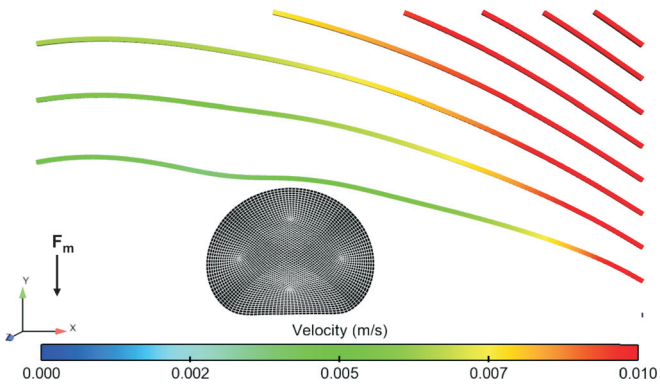

FIG. 12. Fully develop fluid velocity field around the cell (0.4 s after simulation start). The cell has been attracted to the wall and flattened by the magnetic force acting on the cell. The fluid forces result in the slow rolling of the cell during the simulation as the wall of the artery has been modelled as frictionless (see supplementary movie 1).

IV. DISCUSSION

Overcoming fluid forces is of major importance for most magnetic cell or drug targeting approaches. It is therefore important to optimize all important components involved such as cell labeling, magnet actuation device design and delivery protocol. Furthermore, any such study needs to follow a thorough parameter optimization, which will be dependent on the geometry of the targeting tissue. While there is a lot of literature on particle optimization[49–52] and cell loading,[53,54] there is little material documenting magnet optimization.[41,48,55] Additionally previous reports have only tested a small number of geometric arrangements, while we have investigated a wide range of configurations to maximise the potential for translation of a clinical magnet actuation device.

Our optimizations showed that for arteries in the legs, a Halbach cylinder k3 outperforms all other potential arrangements of permanent magnets. This would also be true for other arrangements where the arteries are not close to the skin. It is advantageous that Halbach cylinders produce fields with rotational symmetry as this makes positioning of the magnet straightforward. Linear field gradients produced by the Halbach cylinder k3 lead to constant forces over a wide range where the magnetic particles are fully magnetized. However, this comes with the drawback that the force will fall to zero close to the center. If a human leg is centered in a Halbach cylinder, the peroneal artery will be closest to the center and can cross the centerline (data not shown). This is not desirable as cells might be washed away but clinical experience suggests that the reendothelialization of the posterior and anterior tibial artery is of greater importance.[5] Hence, it might be acceptable to have some areas of the peroneal artery where magnetic cell delivery would be less efficient.

As mentioned above, fluid forces are a major obstacle for magnetic cell and drug targeting. Consequently, it is important to consider them during the optimization process. CFD offers interesting opportunities to study magnetic targeting in fluids. This approach has previously been used for the targeting of magnetic particles in experimental arrangements[29,56,57] but has not been combined with patient derived geometry and blood flow data for the purpose of cell targeting. Our CFD model was built from MR data, which allowed the theoretical assessment of cell targeting efficiency for the human lower leg arteries. For a healthy volunteer the fluid forces were dominant and lead to a targeting efficiency of 6.25% for strongly labeled cells. Cells which were close to the vessel wall ($<0.5\%$ of the radius) were attracted during peak flow even when they experienced only a magnetic force of 12 pN. Only first pass capturing has been considered as cells returning with the venous blood to the heart are likely to be captured in the lung.

In patients with PAD, it is likely that the blood flow rates are lower due to their condition. Additionally cell aggregation due to dipole interactions at the magnetic flux density used is likely to increase targeting efficiency.[58] Nevertheless, we envisage the best delivery protocol would be to stop blood flow for 5 min, while cells are delivered via a catheter which is being retracted. This would increase the targeting efficiency to almost 100%. The leg would be placed in the center of the magnet during cell delivery and kept there for another 30 min to allow cell attachment to the artery; such an approach should be acceptable from a clinical perspective. This initial cessation of blood flow would allow cells to be attracted to the vessel wall. On reperfusion, the low fluid velocities close the boundary permit the magnetic forces to overcome the drag force and thus prevent cells from washing away. Another point which needs to be considered is that due to the positions of the arteries relative to the center of the Halbach cylinder, cells would be attracted to a half circle of the vessel wall covering about 50% of the vessel inner surface. Cells would have to spread out to cover the remaining area.

The strength of the magnetic forces generated is also dependent on the cell labeling. We performed all magnet optimizations assuming a cell loading of 15 pg iron per cell, which is an amount we have previously achieved.[26] For some of the CFD simulations we investigated cells loaded with 150 pg iron. Labeling concentrations between 10 and 300 pg iron per cell have been reported previously,[59,60] which indicates that such labeling efficiencies should be achievable. However, this requires to be tested for the cell line under investigation.

In order to get a better idea of how cells might behave in the boundary layer of the vessel wall, we used a fluid-structure interaction approach. The simulation of a single elastic cell being attracted to a surface by magnetic forces acting on each vertices and fluid flow around the cell led to the flattening of the cell. This flattening together with the magnetic force was sufficient to prevent the cell from flowing away, but it did not stop the cell from slowly rolling along. Such behavior is not surprising as the vessel wall has been modelled as frictionless. However this abstract model highlights that a cell can be held at the vessel wall with magnetic forces from our magnet arrangement. Realistic wall friction and surface receptors on the cells themselves will likely generate friction and increase the strength of the cell attachment to the vessel wall impeding the cells from rolling along. Modelling of the cell as a elastic object increases the contact area between cell and vessel wall, which for the deformable cell would be 30 μm^2 while the contact area for the case of a rigid sphere is essentially a point, resulting in reduced frictional force which leads to a less positive outcome in cell attachment.

One of the major problems for the development of magnetic targeting applications is the poor scalability of magnets. This is a consequence of the inverse square law behavior of magnetic fields, which makes it easy to generate sufficient force at the scale of a small animal but very difficult to do this for a human. This problem has not been addressed sufficiently in the magnetic targeting literature as many experiments performed on small animals cannot be scaled up.[22,61] Nevertheless if theoretical optimizations are first performed with realistic human geometry and blood flow data, a scale down can be possible. We showed that our best performing magnet design could be scaled down for a rabbit arterial injury model such that the forces acting on the

cells would be similar to those generated for human arteries. However, we do admit that force linearity is limited to a smaller range and blood velocities can only be adjusted by selecting an appropriate artery. This choice is additionally restrained by biological considerations.

CFD simulations for the rabbit carotid artery showed that cell capture efficiencies under flow are higher than those estimated for human lower leg arteries. This is mainly due to the lower mean flow rate and the lower diameter. Even so, the scale down would still be valid as the blood flow would have to be stopped for 5 min in the rabbit also. As for the human case, cells would have reached the boundary layer in this time where the magnetic forces would dominate the fluid forces. In this boundary layer, the behavior of cells would be similar for human and rabbit arteries.

V. SUMMARY

For our best performing magnet arrangement (Halbach cylinder k3) the targeting efficiency for all cells passing through the posterior tibial artery during one heart beat was 6.25% (first pass capture). However, if the flow is stopped for 5 min a targeting efficiency of close to 100% could be achieved as magnetic forces would be strong enough to attract and hold cells at the vessel wall potentially increasing cell efficacy. Finally, this magnet can be scaled down for a preclinical rabbit injury model without changing the magnetic force acting on the cell. This leads to similar behavior in the boundary layer close to the vessel wall, thus enabling development and testing of clinically relevant magnetic cell targeting approaches in an animal model.

ACKNOWLEDGMENTS

We would like to thank the endovascular team from the University College London Hospital and Kathryn Broadhouse from the Robert Steiner MRI Unit, Hammersmith Hospital for their assistance. Paul Southern from The Royal Institution of Great Britain for magnetic susceptibility measurements using SQUID. Additionally, we would also like to thank the British Heart Foundation and the Engineering and Physical Sciences Research Council for funding this work.

[a]Author to whom correspondence should be addressed. Electronic mail: j.riegler@ucl.ac.uk
[b]Joint senior authors.

[1]A. T. Hirsch, M. H. Criqui, D. Treat-Jacobson, J. G. Regensteiner, M. A. Creager, J. W. Olin, S. H. Krook, D. B. Hunninghake, A. J. Comerota, M. E. Walsh, M. M. McDermott, and W. R. Hiatt, "Peripheral arterial disease detection, awareness, and treatment in primary care," JAMA J. Am. Med. Assoc. **286**, 1317–1324 (2001).
[2]E. Selvin and T. P. Erlinger, "Prevalence of and risk factors for peripheral arterial disease in the United States: Results from the national health and nutrition examination survey, 1999–2000," Circulation **110**, 738–743 (2004).
[3]American Heart Association, Heart disease and stroke statistics-2004, Dallas (2004).
[4]G. J. Becker, T. E. McClenny, M. E. Kovacs, R. D. Raabe, and B. T. Katzen, "The importance of increasing public and physician awareness of peripheral arterial disease," J. Vasc. Interv. Radiol. **13**, 7–11 (2002).
[5]L. Graziani and A. Piaggesi, "Indications and clinical outcomes for below knee endovascular therapy: Review article," Cathet. Cardiovasc. Intervent. **75**, 433–443 (2010).
[6]C. J. White and W. A. Gray, "Endovascular therapies for peripheral arterial disease: An evidence-based review," Circulation **116**, 2203–2215 (2007).
[7]R. Hoffmann, G. S. Mintz, G. R. Dussaillant, J. J. Popma, A. D. Pichard, L. F. Satler, K. M. Kent, J. Griffin, and M. B. Leon, "Patterns and mechanisms of in-stent restenosis: A serial intravascular ultrasound study," Circulation **94**, 1247–1254 (1996).
[8]R. Kornowski, M. K. Hong, F. O. Tio, O. Bramwell, H. Wu, and M. B. Leon, "In-stent restenosis: Contributions of inflammatory responses and arterial injury to neointimal hyperplasia," J. Am. Coll. Cardiol. **31**, 224–230 (1998).
[9]A. W. Heldman, L. Cheng, G. M. Jenkins, P. F. Heller, D. W. Kim, M. Ware, Jr., C. Nater, R. H. Hruban, B. Rezai, B. S. Abella, K. E. Bunge, J. L. Kinsella, S. J. Sollott, E. G. Lakatta, J. A. Brinker, W. L. Hunter, and J. P. Fröhlich, "Paclitaxel stent coating inhibits neointimal hyperplasia at 4 weeks in a porcine model of coronary restenosis," Circulation **103**, 2289–2295 (2001).
[10]D. Kong, L. G. Melo, A. A. Mangi, L. Zhang, M. Lopez-Ilasaca, M. A. Perrella, C. C. Liew, R. E. Pratt, and V. J. Dzau, "Enhanced inhibition of neointimal hyperplasia by genetically engineered endothelial progenitor cells," Circulation **109**, 1769–1775 (2004).
[11]N. Werner, S. Junk, U. Laufs, A. Link, K. Walenta, M. Bohm, and G. Nickenig, "Intravenous transfusion of endothelial progenitor cells reduces neointima formation after vascular injury," Circ. Res. **93**, e17–e24 (2003).
[12]S. Windecker, I. Mayer, G. De Pasquale, W. Maier, O. Dirsch, P. De Groot, Y. P. Wu, G. Noll, B. Leskosek, B. Meier, and O. M. Hess, "Stent coating with titanium-nitride-oxide for reduction of neointimal hyperplasia," Circulation **104**, 928–933 (2001).
[13]J. Aoki, P. W. Serruys, H. van Beusekom, A. T. L. Ong, E. P. McFadden, G. Sianos, W. J. van der Giessen, E. Regar, P. J. de Feyter, H. R. Davis, S. Rowland, and M. J. B. Kutryk, "Endothelial progenitor cell capture by stents coated with antibody against CD34: The HEALING-FIM (healthy endothelial accelerated lining inhibits neointimal growth-first in man) registry," J. Am. Coll. Cardiol. **45**, 1574–1579 (2005).
[14]B. Lagerqvist, S. K. James, U. Stenestrand, J. Lindbäck, T. Nilsson, and L. Wallentin, "Long-term outcomes with drug-eluting stents versus bare-metal stents in Sweden," N. Engl. J. Med. **356**, 1009–1019 (2007).
[15]T. Asahara, T. Murohara, A. Sullivan, M. Silver, R. van der Zee, T. Li, B. Witzenbichler, G. Schatteman, and J. M. Isner, "Isolation of putative progenitor endothelial cells for angiogenesis," Science **275**, 964–966 (1997).
[16]R. Waksman, R. Baffour, R. Pakala, M. Scheinowitz, D. Hellinga, R. Seabron, R. Chan, F. Kolodgie, and R. Virmani, "Effects of exogenous peripheral-blood-derived endothelial progenitor cells or unfractionated bone-marrow-derived cells on neointimal formation and inflammation in cholesterol-fed, balloon-denuded, and radiated iliac arteries of inbred rabbits," Cardiovasc. Revasc. Med. **10**, 110–116 (2004).
[17]M. Peichev, A. J. Naiyer, D. Pereira, Z. Zhu, W. J. Lane, M. Williams, M. C. Oz, D. J. Hicklin, L. Witte, M. A. S. Moore, and S. Rafii, "Expression of VEGFR-2 and AC133 by circulating human CD34+ cells identifies a population of functional endothelial precursors," Blood **95**, 952–958 (2000).
[18]D. Hou, E. A.-S. Youssef, T. J. Brinton, P. Zhang, P. Rogers, E. T. Price, A. C. Yeung, B. H. Johnstone, P. G. Yock, and K. L. March, "Radiolabeled cell distribution after intramyocardial, intracoronary, and interstitial retrograde coronary venous delivery: Implications for current clinical trials," Circulation **112**, I150–1156 (2005).
[19]F. Pelliccia, C. Cianfrocca, G. Rosano, G. Mercuro, G. Speciale, and V. Pasceri, "Role of endothelial progenitor cells in restenosis and progression of coronary atherosclerosis after percutaneous coronary intervention: a prospective study," J. Am. Coll. Cardiol. Intv. **3**, 78–86 (2010).
[20]A. S. Lübbe, C. Bergemann, H. Riess, F. Schriever, P. Reichardt, K. Possinger, M. Matthias, B. Dorken, F. Herrmann, R. Gurtler, P. Hohenberger, N. Haas, R. Sohr, B. Sander, A. J. Lemke, D. Ohlendorf, W. Huhnt, and D. Huhn, "Clinical experiences with magnetic drug targeting: A phase I study with 4′-epidoxorubicin in 14 patients with advanced solid tumors," Cancer Res. **56**, 4686–4693 (1996).
[21]C. Alexiou, D. Diehl, P. Henninger, H. Iro, R. Rockelein, W. Schmidt, and H. Weber, "A high field gradient magnet for magnetic drug targeting," IEEE Trans. Appl. Supercond. **16**, 1527–1530 (2006).
[22]P. Dames, B. Gleich, A. Flemmer, K. Hajek, N. Seidl, F. Wiekhorst, D. Eberbeck, I. Bittmann, C. Bergemann, T. Weyh, L. Trahms, J. Rosenecker, and C. Rudolph, "Targeted delivery of magnetic aerosol droplets to the lung," Nat. Nanotechnol **2**, 495–499 (2007).

[23]C. Plank, M. Anton, C. Rudolph, J. Rosenecker, and F. Krötz, "Enhancing and targeting nucleic acid delivery by magnetic force," Expert Opin. Biol. Ther. **3**, 745–758 (2003).
[24]S. V. Pislaru, A. Harbuzariu, R. Gulati, T. Witt, N. P. Sandhu, R. D. Simari, and G. S. Sandhu, "Magnetically targeted endothelial cell localization in stented vessels," J. Am. Coll. Cardiol. **48**, 1839–1845 (2006).
[25]B. Polyak, I. Fishbein, M. Chorny, I. Alferiev, D. Williams, B. Yellen, G. Friedman, and R. J. Levy, "High field gradient targeting of magnetic nanoparticle-loaded endothelial cells to the surfaces of steel stents," Proc. Natl. Acad. Sci. U. S. A. **105**, 698–703 (2008).
[26]P. G. Kyrtatos, P. Lehtolainen, M. Junemann-Ramirez, A. Garcia-Prieto, A. N. Price, J. F. Martin, D. G. Gadian, Q. A. Pankhurst, and M. F. Lythgoe, "Magnetic tagging increases delivery of circulating progenitors in vascular injury," JACC: Cardiovasc. Interv. **2**, 794–802 (2009).
[27]A. Weber, I. Pedrosa, A. Kawamoto, N. Himes, J. Munasinghe, T. Asahara, N. M. Rofsky, and D. W. Losordo, "Magnetic resonance mapping of transplanted endothelial progenitor cells for therapeutic neovascularization in ischemic heart disease," Eur. J. Cardiothorac Surg. **26**, 137–143 (2004).
[28]P. J. Cregg, K. Murphy, and A. Mardinoglu, "Inclusion of magnetic dipole-dipole and hydrodynamic interactions in implant-assisted magnetic drug targeting," J. Magn. Magn. Mater. **321**, 3893–3898 (2009).
[29]M. C. Erica, G. M. Peter, and K. E. John, "Particle size, magnetic field, and blood velocity effects on particle retention in magnetic drug targeting," Med. Phys. **37**, 175–182 (2010).
[30]A. Nacev, C. Beni, O. Bruno, and B. Shapiro, "Magnetic nanoparticle transport within flowing blood and into surrounding tissue," Nanomedicine **5**, 1459–1466 (2010).
[31]J. W. M. Bulte, T. Douglas, B. Witwer, S. C. Zhang, E. Strable, B. K. Lewis, H. Zywicke, B. Miller, P. van Gelderen, B. M. Moskowitz, I. D. Duncan, and J. A. Frank, "Magnetodendrimers allow endosomal magnetic labeling and in vivo tracking of stem cells," Nat. Biotechnol. **19**, 1141–1147 (2001).
[32]I. J. de Vries, W. J. Lesterhuis, J. O. Barentsz, P. Verdijk, J. H. van Krieken, O. C. Boerman, W. J. G. Oyen, J. J. Bonenkamp, J. B. Boezeman, G. J. Adema, J. W. M. Bulte, T. W. J. Scheenen, C. J. A. Punt, A. Heerschap, and C. G. Figdor, "Magnetic resonance tracking of dendritic cells in melanoma patients for monitoring of cellular therapy," Nat. Biotechnol. **23**, 1407–1413 (2005).
[33]C. Alexiou, R. Jurgons, R. J. Schmid, C. Bergemann, J. Henke, W. Erhardt, E. Huenges, and F. Parak, "Magnetic drug targeting-biodistribution of the magnetic carrier and the chemotherapeutic agent mitoxantrone after locoregional cancer treatment," J. Drug Target. **11**, 139–149 (2003).
[34]U. O. Häfeli, S. M. Sweeney, B. A. Beresford, J. L. Humm, and R. M. Macklis, "Effective targeting of magnetic radioactive90Y-microspheres to tumor cells by an externally applied magnetic field. Preliminary in vitro and in vivo results," Nucl. Med. Biol. **22**, 147–155 (1995).
[35]S. I. Takeda, F. Mishima, S. Fujimoto, Y. Izumi, and S. Nishijima, "Development of magnetically targeted drug delivery system using superconducting magnet," J. Magn. Magn. Mater. **311**, 367–371 (2007).
[36]M. O. Avilés, A. D. Ebner, and J. A. Ritter, "Implant assisted-magnetic drug targeting: Comparison of in vitro experiments with theory," J. Magn. Magn. Mater. **320**, 2704–2713 (2008).
[37]H. Azuma, N. Funayama, T. Kubota, and M. Ishikawa, "Regeneration of endothelial cells after balloon denudation of the rabbit carotid artery and changes in responsiveness," Jpn. J. Pharmacol. **52**, 541–552 (1990).
[38]D. Y. Hui, "Intimal hyperplasia in murine models," Curr. Drug Targets **9**, 251–260 (2008).
[39]T. A. Painter, "Myointimal hyperplasia: Pathogenesis and implications. 2. Animal injury models and mechanical factors," Artif. Organs **15**, 103–118 (1991).
[40]Q. A. Pankhurst, J. Connolly, S. K. Jones, and J. Dobson, "Applications of magnetic nanoparticles in biomedicine," J. Phys. D: Appl. Phys. **36**, R167–R181 (2003).
[41]K. Halbach, "Design of permanent multipole magnets with oriented rare earth cobalt material," Nucl. Instrum. Methods **169**, 1–10 (1980).
[42]Neodymium-Iron-Boron Magnets. http://www.tdk.co.jp/tefe02/e331.pdf.
[43]Sintered ferrite magnets. http://www.magnetsales.co.uk/sintered-ferrite.htm.
[44]Segment version 1.8R0462 (http://segment.heiberg.se).
[45]E. Heiberg, J. Sjögren, M. Ugander, M. Carlsson, H. Engblom, and H. Arheden, "Design and validation of Segment—freely available software for cardiovascular image analysis," BMC Med. Imaging **10**, 1–13 (2010).
[46]X. Cui, C. Labarrere, L. He, S. Cheng, H. Siderys, R. Kovacs, and D. Gao, "Cryopreservation and microsurgical implantation of rabbit carotid arteries," Cell Preserv. Technol **1**, 121–128 (2002).
[47]H. Sato, M. Katano, T. Takigawa, and T. Masuda, "Estimation for the elasticity of vascular endothelial cells on the basis of atomic force microscopy and Young's modulus of gelatin gels," Polym. Bul1 **47**, 375–381 (2001).
[48]R. Bjørk, C. R. H. Bahl, A. Smith, and N. Pryds, "Optimization and improvement of Halbach cylinder design," J. Appl. Phys. **104**, 013910–013919 (2008).
[49]M. Arruebo, R. Fernández-Pacheco, M. R. Ibarra, and J. Santamará, "Magnetic nanoparticles for drug delivery," Nanotoday **2**, 22–32 (2007).
[50]J. Dobson, "Magnetic nanoparticles for drug delivery," Drug Dev. Res. **67**, 55–60 (2006).
[51]A. Kumar, P. K. Jena, S. Behera, R. F. Lockey, S. Mohapatra, and S. Mohapatra, "Multifunctional magnetic nanoparticles for targeted delivery," Nanomedicine **6**, 64–69 (2009).
[52]R. S. Molday, S. P. S. Yen, and A. Rembaum, "Application of magnetic microspheres in labelling and separation of cells," Nature (London) **437**–438 (1977).
[53]A. S. Arbab, G. T. Yocum, A. M. Rad, A. Y. Khakoo, V. Fellowes, E. J. Read, and J. A. Frank, "Labeling of cells with ferumoxides-protamine sulfate complexes does not inhibit function or differentiation capacity of hematopoietic or mesenchymal stem cells," NMR Biomed. **18**, 553–559 (2005).
[54]E. M. Shapiro, L. N. Medford-David,T. M. Fahmy, C. E. Dunbar, and A. P. Koretsky, "Antibody-mediated cell labeling of peripheral T cells with micron-sized iron oxide particles (MPIOs) allows single cell detection by MRI," Contrast Media Mol. Imaging **2**, 147–153 (2007).
[55]U. O. Häfeli, K. Gilmour, A. Zhou, S. Lee, and M. E. Hayden, "Modeling of magnetic bandages for drug targeting: Button vs. Halbach arrays," J. Magn. Magn. Mater. **311**, 323–329 (2007).
[56]P. J. Cregg, K. Murphy, A. Mardinoglu, and A. Prina-Mello, "Many particle magnetic dipole-dipole and hydrodynamic interactions in magnetizable stent assisted magnetic drug targeting," J. Magn. Magn. Mater. **322**, 2087–2094 (2010).
[57]J. Ally, B. Martin, M. Behrad Khamesee, W. Roa, and A. Amirfazli, "Magnetic targeting of aerosol particles for cancer therapy," J. Magn. Magn. Mater. **293**, 442–449 (2005).
[58]J. Riegler, B. Allain, R. J. Cook, M. F. Lythgoe, and Q. A. Pankhurst, "Magnetically assisted delivery of cells using a magnetic resonance imaging system," J. Phys. D: Appl. Phys. **44**, 055001–055011 (2011).
[59]J. Riegler, J. A. Wells, P. G. Kyrtatos, A. N. Price, Q. A. Pankhurst, and M. F. Lythgoe, "Targeted magnetic delivery and tracking of cells using a magnetic resonance imaging system," Biomaterials **31**, 5366–5371 (2010).
[60]K. A. Hinds, J. M. Hill, E. M. Shapiro, M. O. Laukkanen, A. C. Silva, C. A. Combs, T. R. Varney, R. S. Balaban, A. P. Koretsky, and C. E. Dunbar, "Highly efficient endosomal labeling of progenitor and stem cells with large magnetic particles allows magnetic resonance imaging of single cells," Blood **102**, 867–872 (2003).
[61]H. Chen, M. D. Kaminski, P. Pytel, L. Macdonald and A. J. Rosengart, "Capture of magnetic carriers within large arteries using external magnetic fields," J. Drug Target. **16**, 262–268 (2008).
[62]See supplementary material at E-MPHYA6-38-049106 for a movie showing the behavior of a magnetically labelled cell close to the vessel wall. For more information on EPAPS, see http://www.aip.org/pubservs/epaps.html